**Atmospheric
Measurement
Techniques
Discussions**

Raman Lidar for Meteorological Observations, RALMO – Part I: Instrument description

T. S. Dinoev[1,*]**, V. B. Simeonov**[1]**, Y. F. Arshinov**[2,†]**, S. M. Bobrovnikov**[2]**,
P. Ristori**[1,3]**, B. Calpini**[4]**, M. B. Parlange**[1]**, and H. van den Bergh**[5]

[1]Laboratory of Environmental Fluid Mechanics and Hydrology (EFLUM), Ecole Polytechnique Fédérale de Lausanne EPFL-ENAC, Station 2, 1015 Lausanne, Switzerland
[2]V.E. Zuev Institute of Atmospheric Optics SB RAS1, Academician Zuev square Tomsk, 634021, Russia
[3]División Lidar, CEILAP (UNIDEF-CITEDEF-MINDEF-CONICET) San Juan Bautista de La Salle 4397 (B1603ALO) Villa Martelli, Buenos Aires, Argentina
[4]Federal Office of Meteorology and Climatology MeteoSwiss, Atmospheric Data, P.O. Box 316, 1530 Payerne, Switzerland
[5]Laboratory of Air and Soil Pollution, Ecole Polytechnique Fédérale de Lausanne EPFL, Station 6, 1015 Lausanne, Switzerland
[*]now at: A private company
[†]deceased

AMTD

5, 6867–6914, 2012

RALMO Part I: Instrument description

T. S. Dinoev et al.

RALMO Part I: Instrument description

T. S. Dinoev et al.

Title Page

Abstract | Introduction

Conclusions | References

Tables | Figures

|◄ | ►|

◄ | ►

Back | Close

Full Screen / Esc

Printer-friendly Version

Interactive Discussion

Abstract

A new Raman lidar for unattended, round the clock measurement of vertical water vapor profiles for operational use by the MeteoSwiss has been developed during the past years by the Swiss Federal Institute of Technology- Lausanne. The lidar uses narrow-field-of-view, narrow-band configuration, a UV laser, and four 30 cm in diameter mirrors, fiber-coupled to a grating polychromator. The optical design allows water vapor retrieval from the incomplete overlap region without instrument-specific range-dependent corrections. The daytime vertical range covers the mid-troposphere, whereas the night-time range extends to the tropopause. The near range coverage is extended down to 100 m AGL by the use of an additional fiber in one of the telescopes. This paper describes the system layout and technical realization. Day and night time lidar profiles compared to Vaisala RS-92 and Snow White® profiles and a six-day-continuous observation are presented as an illustration of the lidar measurement capability.

1   Introduction

Water vapor plays a fundamental role in the radiative energy transfer, hydrological cycle, and atmospheric chemistry processes that determine weather and climate. It influences the radiative budget of the planet both directly and through coupling with clouds. Because of its strong absorption and emission bands, especially in the infrared, and because of its abundance, water vapor is the most significant greenhouse gas, and in this sense the most important in establishing the Earth's climate.

Water vapor distribution is strongly affected by atmospheric dynamics, but in turn, it also influences atmospheric circulation and temperature structure by condensation-evaporation processes. The water evaporation-condensation cycle is an important mechanism for transferring heat energy from the Earth's surface to the atmosphere and in moving heat around the Earth. The large latent energy associated with the water phase changes significantly affects the meridional energy balance and the vertical

stability of the atmosphere, as well as, the structure and evolution of storm systems, not only in the boundary layer (Normand, 1938), but also in the middle and upper troposphere (Peppler, 1989; Sinha, 1995; Arnold, 2008).

Because of its essential role in the atmospheric processes, the water vapor spatial distribution and its temporal evolution are two of the most important parameters in global and regional numerical weather prediction (NWP) models. To improve near-surface weather predictions, and to better simulate the evolution of local severe weather events in complex terrains (Wulfmeyer, 2008), the time and space resolution of the NWP models is currently being increased. The vertical water vapor profiles assimilated by these models are mainly acquired by twice-a-day radiosonde observations which however have insufficient time resolution to resolve fast running meteorological phenomena. In addition, radiosonde measurements suffer from difficult to correct systematic errors and essential sonde-to-sonde variations not only between instruments from different producers and operational principles, but even between instruments of the same batch (Nash, 2010). Ground based microwave radiometers (Solheim, 1998 and references therein) or Fourier transform infrared radiometers (Schneider, 2009 and references therein) provide humidity profiles with sufficient time resolution, but with rather low vertical resolution, insufficient to resolve the spatial variability of water vapor in the low troposphere. Therefore, new operational instruments for near-real time observations of the tropospheric water vapor field are needed.

Lidar (light detection and ranging) is one of the techniques able to resolve the high temporal and spatial variability of tropospheric water vapor. The advances during the last decades in the field of laser technology and improved lidar design make lidars suitable for operational use. Two lidar techniques, DIAL and Raman are used for water vapor measurements.

The DIAL principle exploits the difference in atmospheric extinction due to water vapor absorption at two closely-spaced, near-IR wavelengths. Provided accurate knowledge of water vapor absorption cross section is available, DIAL does not need other external references for correct measurements and in this sense is considered

Title Page

Abstract | Introduction

Conclusions | References

Tables | Figures

◄ | ►

◄ | ►

Back | Close

Full Screen / Esc

Printer-friendly Version

Interactive Discussion

"self-calibrating". A single-wavelength DIAL system has the potential to perform daytime observations with high temporal resolution but limited altitude range (2–3 km) when operated from low-altitude, ground-based sites because the humid air in the boundary layer significantly attenuates the laser beam (Wulfmeyer, 1998). The need for an expensive and sophisticated tunable laser source and the complicated data treatment is another obstacle for implementing DIAL as an operational, ground based instrument for meteorology. This technique, however, is well suited for airborne and satellite profiling (Browell, 1998; Bruneau, 2001; Wirth, 2009).

The Raman lidar technique exploits Raman scattering from water vapor and nitrogen molecules to derive a profile of water vapor mixing ratio (Cooney, 1970; Melfy, 1972). At present, the night-time distance range can reach the lower stratosphere but at daytime the range is limited to the middle troposphere because the weak Raman signals are detected in the presence of intensive daylight background. A Raman lidar requires calibration either against a reference instrument or by absolute radiometric calibration of the lidar optics, provided accurate Raman cross sections are available. Contrary to a DIAL, a Raman lidar does not require tunable laser source with specific and highly stabilized wavelengths. Furthermore, the Raman data-treatment algorithm is significantly simpler than the DIAL algorithm, and allows data retrieval from the incomplete overlap region. Because of all these advantages and because of the higher reliability, Raman lidars are preferred for operational use in meteorology from ground-based stations (Goldsmith, 1998; Engelbart, 2006; Simeonov, 2010; Apituley, 2006).

Raman lidars have been used for high-resolution vertical profiling of water vapor within the troposphere since the early 70ies of the last century. Most of the measurements were performed for research purposes and at night time (Whiteman, 1992; Ansmann, 1992; Vaughan, 1998; Balin, 2004). First daytime measurements were possible using laser wavelength shorter than 300 nm because at these wavelengths the solar light is absorbed by stratospheric ozone (Renault, 1980; Cooney, 1985). The vertical range of such lidars is however, limited to about 2 km, mainly due to tropospheric ozone absorption. The use of a narrow field-of-view (NFOV), narrow band (NB) receiver allows

operation at visible and near UV wavelengths with distance range extended up to the mid troposphere (Goldsmith, 1998).

The successful long-term operation of the first automated NFOV, NB lidar – CART (Goldsmith, 1998) motivated the German (Engelbart, 2006), the Swiss (Simeonov, 2010) and the Dutch (Appituley, 2006) meteorological services to establish programs aiming at the development of operational water vapor lidars.

Here we present the instrument description and results from the Swiss Raman lidar for meteorological observations, RALMO. RALMO was developed and built by the Swiss Federal Institute of Technology-Lausanne (**E**cole **P**olytechnique **F**ederale de **L**ausanne-EPFL) as a co-funded project with the Swiss Meteorological Office (MeteoSwiss) and supported by the Swiss National Foundation. The lidar is operated at the aerological station in Payerne by MeteoSwiss with the support of EPFL. RALMO is dedicated to operational meteorology, model validation, as well as, ground truthing of satellite data. It provides regular water vapor profiles with high spatial and temporal resolution in near-real-time, thus improving the database for near-real-time meteorological applications. Long-term system stability and homogeneity of the emerging water vapor data set is an important goal of the RALMO program and climate monitoring is considered a perspective application of this instrument. RALMO increases the capacity of the Payerne observatory to measure water vapor in the troposphere and reinforces its role as a GRUAN station and a CIMO testbed.

The article is structured as follows: the physical principles of Raman remote sensing of water vapor are summarized in Sect. 2. A detailed description of the instrument follows in Sect. 3, and the data processing and calibration, as well as example results are presented in Sect. 4.

2 Theory of operation

The operation is based on the well-known Raman lidar principle where a humidity profile is derived from the water vapor and nitrogen Raman components of atmospheric

laser backscatter (Cooney, 1970; Melfi, 1972). In a single scattering approximation, the power of the Raman lidar signal per pulse, and from altitude z is:

$$P_x(z) = E \frac{AO_x(z)}{z^2} \frac{c}{2} \eta_x \sigma_x^\pi(\lambda, T) N_x(z) \Delta\tau_x^{\mathrm{aer}}(z) \Delta\tau_x^{\mathrm{mol}}(z) + P_{\mathrm{B}x} \tag{1}$$

where E is the laser energy per pulse, A is the telescope surface, $O_x(z)$ is the overlap function, η_x is the total efficiency of the lidar receiver for the respective wavelength and $\sigma_x^\pi(\lambda, T)$ is the Raman cross section of species x with number density $N_x(z)$, where T is the temperature of the probed volume. The attenuation of the laser beam and the Raman backscattered light due to aerosol scattering and absorption is accounted for in $\Delta\tau_x^{\mathrm{aer}}(z)$, and $\Delta\tau_x^{\mathrm{mol}}(z)$ is the molecular attenuation. The additional term $P_{\mathrm{B}x}$ is the power of the sky background (Measures, 1992):

$$P_{\mathrm{B}x} = R_x(\lambda) A \Omega \Delta\lambda_x \tag{2}$$

where $R_x(\lambda)$ is the zenith sky spectral radiance, Ω is the field-of-view of the telescope, expressed as a solid angle, and $\Delta\lambda_x$ is the spectral transmission bandwidth (FWHM) of the detection channel. In daytime conditions, the lidar receiver detects considerable amount of diffuse sky light, which influences the daytime performance of the lidar by significantly reducing the signal-to-noise-ratio (SNR) of the Raman signals. The daylight influence can be reduced using a narrow field-of-view receiver and a polychromator with narrow band, which isolates only the Q branch of the ro-vibrational spectra of the signals (Goldsmith, 1999).

A vertical profile of the water vapor mixing ratio $q(z)$ is derived from the ratio of the water vapor to nitrogen lidar signals as:

$$q(z) = nC_{\mathrm{L}} \frac{\overline{P_{\mathrm{H_2O}}(z)}}{\overline{P_{\mathrm{N_2}}(z)}} \Delta\tau(z) \tag{3}$$

where the signals $\overline{P_{\mathrm{H_2O}}(z)}$ and $\overline{P_{\mathrm{N_2}}(z)}$ are background-corrected and averaged over time and range to reduce the statistical error. The coefficient $n = 0.485$ converts the obtained

through lidar measurements water vapor to nitrogen mixing ratio to water vapor to dry air mixing ratio, $\Delta\tau(z)$ is the one-way differential atmospheric transmission at water vapor and nitrogen wavelengths and depends on the profiles of the aerosol $\Delta\alpha^{a}(z) = \alpha^{a}_{H_2O}(z) - \alpha^{a}_{N_2}(z)$ and molecular $\Delta\alpha^{m}(z) = \alpha^{m}_{H_2O}(z) - \alpha^{m}_{N_2}(z)$ differential extinctions as:

$$\Delta\tau(z) = \exp\left\{ -\int_0^z [\Delta\alpha^{m}(z') + \Delta\alpha^{a}(z')]dz' \right\} \tag{4}$$

The molecular extinction is usually calculated from atmospheric pressure and temperature profiles, measured by balloon sounding or derived from an atmospheric model (usually US Standard Atmosphere). The error in water vapor concentration due to aerosol extinction is below 10 % even for hazy conditions (Whiteman, 1992, 2001) and usually can be neglected. If necessary, the aerosol extinction profiles can be obtained from Raman lidar measurements (Ansmann, 1992). The lidar calibration function C_L can be expressed as:

$$C_L(z, \lambda, T) = \frac{O_{N_2}(z)}{O_{H_2O}(z)} \frac{t_{N_2}}{t_{H_2O}} \frac{\eta_{N_2}}{\eta_{H_2O}} \frac{\int \sigma^{\pi}_{N_2}(\lambda, T) I_{N_2}(\lambda)d\lambda}{\int \sigma^{\pi}_{H_2O}(\lambda, T) I_{H_2O}(\lambda)d\lambda} \tag{5}$$

where, t_x is the total wavelength-independent optical transmission of the detection channel x, $I_x(\lambda) \in [0,1]$ is the polychromator instrumental function and η_x is the photodetector quantum efficiency.

As can be seen from Eq. (5), C_L depends directly on the distance only through the overlap functions and only in the incomplete overlap region. In real systems however, all terms in Eq. (5) could and often depend indirectly on the distance. As a result, C_L is in general range dependent. Usual practice in such cases is to present C_L as a product of a range-independent part, referred to as calibration constant, and range dependent corrections usually called "overlap" and "temperature" corrections (Whiteman, 1992, 2003, 2001; Goldsmith, 1998). The term "overlap correction" stems from the fact that the range dependence is more pronounced in the incomplete overlap region. In

the absence of chromatic aberrations (lateral or axial) of the lidar telescope, the two overlap functions, defined at the telescope output aperture, are identical and cancel out because the two Raman signals are produced by the same laser beam. Since the telescopes of most, if not all, Raman lidars are of reflective type (i.e. virtually free

5 from chromatic aberrations), the reason for the range dependence of C_L is the indirect range-dependence of the other three terms. Range independence of C_L, sufficient for accurate measurements, can be achieved by a suitable lidar design. Below we summarize the main reasons leading to range dependence of C_L and in the following sections we give details on the design solutions that allow achieving the sufficient for accurate

10 observation range independence of C_L of our lidar.

Possible reasons for the range-dependence of the remaining terms of Eq. (5) include: differences in the angular dependence of the transmissive reflective or polarisation properties of the optical elements at the two Raman wavelengths; chromatic aberrations; light-spot "traveling" on the surfaces of the optical elements, and vignetting of

15 the optical beams after the telescope output. A range dependence of C_L due to the photodetector imperfections can arise from spatial inhomogeneity of the photomultipliers active surfaces (Simeonov,1999), detector nonlinearities, or signal induced noise.

Another indirect source of range dependence of C_L, compensated by the "temperature" correction, is the temperature sensitivity of the Raman cross-sections $\sigma_x^\pi(\lambda, T)$

20 (Avila, 1999; Whiteman, 2003). The water vapor cross section is more strongly affected because of the more complex structure, respectively spectrum of the water molecule. As seen from Eq. (5), C_L depends on the temperature (range) through the integral of the product of the Raman cross section and the instrumental function:

$$f_x = \int \sigma_x^\pi(\lambda, T) I_x(\lambda) \mathrm{d}\lambda \qquad (6)$$

25 Reducing the temperature dependence of C_L to around 1 % or below can be achieved by selecting the bandwidth and the central wavelength of the instrumental functions, as will be shown below. If the instrumental functions and the atmospheric temperature

profile are well known, temperature corrections could be applied as well (Whiteman, 2003, 2011).

Finally, we have to mention range-dependent errors not related to C_L, but resulting from the lidar design. These error sources lead to range dependent wet bias and can be caused by a leak of light to the water channel at the laser, Raman-shifted nitrogen or oxygen wavelengths, as well as by fluorescence of the receiver optics (Sherlock, 1999; Whiteman, 2011). Another reason for the range dependence, not included in Eq. (5) and pronounced mostly in the incomplete overlap region, is the time difference between the two Raman signals. Such a difference could be due to: a difference in the optical paths; different time responses of the detectors and/or the acquisition system, or differences in the triggering of the acquisition system channels.

3 Instrument description

To satisfy the requirements for operational use in a meteorological network, a water vapor lidar has to meet a number of criteria, the most important of which are listed below: daytime and nighttime measurements covering the middle and the high tropo-sphere, respectively; accuracy and precision of the measured parameters; traceabil-ity of the measurement; near-real-time data availability, long-term data consistency; long-term system stability; autonomous operation, minimal maintenance by a techni-cian; and eye safety. All these requirements were taken into account during the design phase of the lidar construction. The specific design features of the lidar are summarized in the following paragraphs and presented in details in the next sections.

The lidar uses a narrow-band, narrow-field-of-view configuration and an excitation laser operating at 355 nm in order to ensure daytime operation. The receiver telescope consists of four, 30 cm in diameter mirrors, fiber-coupled to a grating polychromator. Extension of the operational range in the lower part of the profile down to 100 m is achieved by using incomplete overlap signals and two fibers in one of the telescopes. The second fiber is collecting signals from distances close to the lidar. The need for

range-dependent corrections is eliminated by the careful design of the receiver, which removes the range dependence of the instrumental part of the lidar calibration constant (Eq. 5). Elimination of the range-dependent corrections not only simplifies the data treatment and calibration but also allows accurate humidity measurements in the case of transmitter-receiver misalignment but at the price of reduced distance range (or precision). To achieve long-term data consistency a grating-based, instead of interference-filter-based polychromator is used. The compact and rigid mechanical design of the lidar, together with the fiber-optic connection between the lidar telescope and the polychromator, ensures long-term alignment stability and eliminates the need for frequent transmitter-receiver alignments.

Figure 1 shows the general optical layout of the lidar, whereas the main lidar parameters are summarized in Table 1 and design details are given in the following sections. The mechanical setup of the lidar and a photo of the telescope are shown in Figs. 2 and 3, respectively. Two computers ensure the automatic operation of the lidar. The first computer controls the lidar hardware and data acquisition, whereas the second one is used for automated data treatment and data transfer. The lidar is installed in a dedicated, clean compartment of an air-conditioned cabin. Four tilted windows, installed above the telescope mirrors, and one horizontal window above the beam expander ensure the weather tightness of the cabin. The cabin is located in a hangar equipped with a sliding roof hatch. The lidar requires only a power supply and a LAN connection for data upload.

3.1 Transmitter

The transmitter is based on a frequency tripled, *Q*-switched Nd:YAG laser (Continuum Powerlite II 9030), supplying up to 400 mJ energy per pulse at 354.7 nm, at 30 Hz repetition rate with 8 ns pulse duration. To extend the flash-lamps lifetime from 20 to approximately 60 million shots, the laser is operated at 300 mJ energy per pulse. The laser was additionally equipped with an energy meter for monitoring the output energy at the third harmonic.

The laser beam is expanded, firstly to reduce the beam divergence which is needed for daytime operation, and secondly to achieve the required for eye-safe operation irradiance decrease. The beam expander is a 15× Galilean type, consisting of two fused-silica lenses: a negative meniscus lens at the input and an aspheric, plano-convex lens at the output (Institute of Atmospheric Optics, Tomsk, Russia). Both lenses are AR coated (SLS Optics Ltd.) for improved expander efficiency. The beam from the laser is directed to the expander input with a fused-silica Pellin-Broca prism. The input and output surfaces of the prism are oriented at Brewster angle, and the laser polarization is rotated with a multiple-order, half-wave plate, installed before the prism to minimize the Fresnel losses on the prism surfaces. The beam steering before the expander reduces the laser beam- receiver misalignment, thus improving the alignment stability of the lidar. This misalignment can be caused by laser pointing instability, laser misalignment or displacement of the laser versus the expander. The use of a prism instead of a dielectric mirror improves the reliability of the lidar and prevents back-reflected from the expander residual IR radiation from reaching the laser.

Ray tracing analysis of the beam expander, taking into account the specified lens aberrations, predicts a reduction of the specified by the laser producer 0.5 mrad beam divergence to approximately 0.06 mrad (full angle), and expansion of the beam diameter from 9 mm to approximately 140 mm. The measured beam divergence shows values of 0.090 ± 0.020 mrad. The difference between the modeled and measured output divergence can be explained by unaccounted lens aberrations or beam expander misalignment.

According to the IEC 60825-1standard, "Safety of laser products", the expanded beam is eye and skin safe for exposure times shorter than 5 s for altitudes below 400 m, whereas above 400 m the safe exposure time increases.

Title Page

Abstract | Introduction

Conclusions | References

Tables | Figures

◄ | ►

◄ | ►

Back | Close

Full Screen / Esc

Printer-friendly Version

Interactive Discussion

3.2 Receiver

3.2.1 Telescope assembly

The lidar receiver uses four, 30 cm in diameter, f/3.33 parabolic mirrors (Institute of Atmospheric Optics, Tomsk, Russia) for collecting the backscattered light. Short fo-
cal length mirrors were chosen because they allow: coupling between the telescope and the polychromator with small core-diameter fibers, and compact telescope design. Furthermore, the comparatively small diameter of the mirrors makes possible the use of dielectric coatings with reflectivity better than 99 % for the wavelength range 375–410 nm and AR coated protective windows (both by SLS Optics Ltd.). The mirrors are
tightly arranged around the beam expander (Figa. 1, 2 and 3) in a robust assembly with a cross section of 0.7 × 0.7 m and height of 1 m. The telescope assembly and the laser head are mounted on a frame welded from square stainless steel tubing. The frame is fixed to the cabin floor with vibration isolators for improving the lidar alignment stability. The rigid and compact transmitter-receiver design reduces the possibility for mechani-
cal and thermal lidar misalignment. Multimode 0.22 NA, UV-enhanced (Ceram Optec$^®$) fused silica fibers, installed near the mirrors focal planes, transmit the collected light to the entrance of the lidar polychromator. The fibers core diameter of 0.2 mm defines a 0.2 mrad FOV of the receiver. Long-pass, edge filters (Semrock$^®$ REF 364) with cutoff wavelength of 363.8 nm and transmission of 10^{-6} at 354.7 nm are installed in front of
the optical fibers. The filters prevent the strong elastic backscatter light from entering the fibers, thus eliminating any possible fiber fluorescence and consequent artifacts. The filters contribute also to the total rejection of the elastic light in the Raman chan-nels.

The receiver is aligned by tilting the individual parabolic mirrors and displacing the
fiber ends towards and away from the mirrors. Kinematic mounts with differential screws are used to tilt each mirror axis within and across a plane defined by the mirror center and the expander axis. The axial displacement of the fibers is performed by holders

Title Page

Abstract | Introduction

Conclusions | References

Tables | Figures

|◄ | ►|

◄ | ►

Back | Close

Full Screen / Esc

Printer-friendly Version

Interactive Discussion

equipped with differential screws. To detect potential signal loss in the far range, we use the product of the overlap function with the two-way aerosol transmission profile, derived from the nitrogen Raman signal.

The full overlap of the receiver is reached at approximately 5 km for fibers positioned at 0.1 mm behind the focus (focusing at 10 km) and mirror axes parallel to the beam expander axe. To increase the signal level and improve the signal-to-noise ratio below 5 km, we tilt the mirrors in the direction of the expander at 35 µrad, which results in full overlap at approximately 3 km. Modeled overlap functions of a single mirror for several tilt angles are presented in Fig. 4. The overlap functions were calculated by ray-tracing (OSLO$^{®}$) assuming flat-top energy distribution of the laser beam. An overlap function, derived from a nitrogen Raman signal measured by the system at mirror tilt angle of 35 µrad, is presented for comparison. A tilt with more than 45 µrad results in slight loss of full overlap at about 10 km, whereas the lidar does not reach full overlap at any distance for tilt angles ≥ 60 µrad.

As seen from Fig. 4, the increase of the tilting angle above 35 µrad does not lead to significant lowering of the full overlap region and the overlap value is close to zero for altitudes below 500 m. To extend the operational distance of the lidar down to 150 m, we use signals from the incomplete overlap region and the signal level below 1 km is enhanced by using an additional fiber, as will be described in the following section.

Deriving water vapor mixing ratio using the incomplete overlap region is possible since the Raman backscatter is excited by a single monochromatic beam and the reflective type lidar telescopes used in our design. Hence, the ratio of overlap functions (Eq. 5) at the telescope output (respectively fiber input) is range independent for any altitude. Possible deviation from the range independence could stem from the chromatic aberrations introduced by the telescope protective windows and from the edge filters, installed before the fibers. The ray tracing estimation shows that the 20 mm thick, fused-silica windows, installed at 15° to the mirrors optical axes, introduce negligible lateral color (less than 0.1 µm) for water vapor and nitrogen wavelengths and practically do not influence the range independence of the overlap ratio. The ratio is

practically range-independent even for observations taken from tens of meters, when the chromatic focal shift due to the divergence of the incident on the windows radiation increases. The edge filters are deposited on 3 mm thick, fused silica substrates and installed in front of the fibers in a convergent beam (f/3.33 telescopes). Ray-tracing indicates 5 µm chromatic focal shift, which has negligible influence on the ratio of ray-traced overlaps at the considered wavelengths. In conclusion, there are no important chromatic aberrations for the current telescope receiver design and the overlap ratio can be considered range-independent. The range independence of the other terms of Eq. (5), which includes the parameters of the spectral separation and detection unit, will be evaluated in the corresponding sections.

3.2.2 Extension of near range coverage

As seen from Fig. 4, the value of the overlap function is close to zero at altitudes below 500 m because of the narrow FOV and the non-coaxial configuration of the lidar. As a result, the near-range signal-to-noise ratio is low and does not allow daytime water vapor retrieval with statistical error lower than 10 % below 225 m. Two methods are usually used to extend the operational distance to lower altitudes: an additional receiver, including an additional telescope and a polychromator (Engelbart, 2006) or a dual field-of-view telescope with an additional polychromator (Goldsmith, 1998). Since both methods increase the complexity of the lidar, reduce its reliability and complicate the data processing we developed a new approach to extend the near range coverage. In this approach, improvement of the near range collection efficiency is achieved by using of an additional, "near range" (NR) fiber, in one of the telescopes. The NR fiber is laterally displaced from the primary fiber in direction opposite to the beam expander at a position where the blurred image of the laser beam, coming from distances close to the lidar, is formed as shown in Fig. 5.

Simulated lidar signals in terms of a range-corrected effective receiver aperture $AO(z)/z^2$ are shown in Fig. 6. The overlap functions are calculated by ray-tracing for mirror tilt of 35 µrad, and fiber positions of 0.1 mm behind the focal plane (focusing at

10 km). Due to the fiber displacement, the NR fiber signal is higher than the principal fiber signal within the range 50 m–800 m in the case of one telescope. The signals from the four telescopes, together with the additional NR signal, are optically summed on the respective photomultiplier cathodes .The resulting "sum" signals with and without NR fiber, presented in Fig. 6 clearly show the contribution of the NR fiber below 1 km.

The use of a NR fiber enhances the near range signal level, but simultaneously increases daylight background, thus reducing the daytime SNR of the far range. To evaluate the influence of the NR fiber on near and far range measurements, we calculated the day-time detection limit of the lidar. The detection limit is defined as the mixing ratio measured with relative error of 10 % (or SNR = 10). Only the water vapor signal is considered in the analysis, since the detection limit is defined mostly by its SNR. The signal variance is estimated using Poisson statistics, and the relative mixing ratio error is:

$$\frac{\partial q}{q}(z) \approx \frac{\sigma_{wv}}{S_{wv}}(z) = \frac{\sqrt{S_{wv}(z) + B_{wv}}}{S_{wv}(z)} \frac{1}{\sqrt{n}}, \tag{7}$$

where $S_{wv}(z)$ is the water vapor Raman lidar signal in terms of count rate, B_{wv} is the light background, and n is the product of the number of averaged spatial bins and the number of laser shots. The Raman signal is calculated, using ray-traced overlaps, molecular two-way transmission from US standard atmosphere, aerosol profile with a constant extinction up to 1 km of 0.16 km^{-1} at 550 nm, and Angström coefficient of 1.4. The daylight background is taken as 65 MHz (per 25 ns detection bin), a value typical for the water vapor signal acquired with the lidar around 2008 summer solstice. This background corresponds to sky zenith radiance of approximately 15 mW cm^{-2} sr^{-1} µm^{-1} at the water vapor wavelength, assuming total channel efficiency of 6.8 % and bandwidth of 0.3 nm.

The modeled daytime detection limits, with and without NR fiber, are compared in Fig. 7 for time averaging of 30 min and spatial averaging of 15 m below, and 300 m above 1 km. The detection limit without the NR fiber is 8.5 g kg^{-1} at 150 m and

increases to more than $10\,\mathrm{g\,kg^{-1}}$ for lower altitudes, a value insufficient for valuable measurements within the first 150 m. The use of a NR fiber reduces the detection limit to less than $1\,\mathrm{g\,kg^{-1}}$ at 150 m, $3\,\mathrm{g\,kg^{-1}}$ at 75 m and to values above $10\,\mathrm{g\,kg^{-1}}$ below 50 m. The right plot of Fig. 7 presents the corresponding detection limit profiles for
5 altitudes above 1 km. The detection limit at 5 km without the NR fiber is $0.65\,\mathrm{g\,kg^{-1}}$ and increases slightly to about $0.71\,\mathrm{g\,kg^{-1}}$ with the fiber. Space averaging of 600 m reduces these values to $0.42\,\mathrm{g\,kg^{-1}}$ without and to $0.46\,\mathrm{g\,kg^{-1}}$ with the NR fiber. The decrease in detection limit could be compensated by increasing the laser output power with approx. 10 %, (operation of the laser at nominal output energy) if necessary.

10 ## 3.2.3 Spectral unit

To achieve long-term data consistency, system stability and negligible range dependence of the calibration constant, the Raman signals are spectrally isolated by a fiber-coupled grating polychromator. The use of a grating-based, instead of a filter-based, polychromator eliminates the long-term gradual shift of the central wavelength and
15 any changes in the transmission related to the interference filter based devices. Furthermore, grating polychromators, contrary to interference-filter based polychromators, allow easy selection of the central wavelength position and bandwidth, hence optimization of the efficiency and minimization of the systematic errors related to the temperature dependence of the Raman cross sections.
20   The polychromator is designed for narrow band isolation of the Q-branches of ro-vibrational water vapor and nitrogen Raman spectra with high-throughput. Special attention was paid to reduce the temperature dependence of C_L by selecting the bandwidth and the central wavelength of the water vapor channel, thus minimizing $f_\mathrm{H_2O}$ (Eq. 6) temperature variations. Figure 8 shows the minimal variations of $f_\mathrm{H_2O}$ in per-
25 cents, with respect to its value at 0 °C, for the temperature interval $-60\,°\mathrm{C} + 40\,°\mathrm{C}$ as a function of the water channel FWHM bandwidth. The minimum values of $f_\mathrm{H_2O}$ are

RALMO Part I: Instrument description

T. S. Dinoev et al.

Title Page

Abstract	Introduction
Conclusions	References
Tables	Figures

◄◄	►►
◄	►
Back	Close

Full Screen / Esc

Printer-friendly Version

Interactive Discussion

T. S. Dinoev et al.

Title Page

Abstract | Introduction

Conclusions | References

Tables | Figures

|◀ | ▶|

◀ | ▶

Back | Close

Full Screen / Esc

Printer-friendly Version

Interactive Discussion

obtained by varying the central wavelength using spectral data from Avila et al. (1999) and Gaussian instrumental function.

As seen from Fig. 8, the f_{H_2O} variations are 1 % or less for bandwidths larger than 0.25 nm. The optimal central wavelength for these bandwidths is around 407.45 nm and varies slightly with the bandwidth. We have chosen the bandwidth of 0.33 nm centered at 407.45 nm which is a compromise between the signal and the day-light noise levels. The nitrogen and oxygen slits are centered at 386.7 nm and 375.4 nm correspondingly. The water vapor spectral transmission function (center wavelength and bandwidth) defines negligible temperature dependence of the transmitted intensity, whereas in the nitrogen channel the relative change of the transmitted intensity is 0.4 %/100 K (Whiteman, 2003), which can also be considered negligible.

The polychromator optical layout is presented in Fig. 9. The optical fibers, delivering the light from the telescopes, are arranged vertically and act as a polychromator entrance slit. The effective slit width and height are defined by the fiber core and external diameter and are respectively 0.2 mm, and 1.1 mm. The three-lens collimator (L1-L2) with an effective focal length of 165 mm (f/2.39) is designed with standard plano-convex spherical lenses. The pre-collimating lens L1 matches the f-numbers of the fiber and the spherical doublet L2. The position of L1 is optimized with the OSLO® ray-tracing program for minimum aberrations. The collimated beam is projected onto a 3600 mm^{-1} blazed holographic grating (Carl Zeiss AG) installed at incidence angle of 35.7° (diffraction angle 62° at water vapor wavelength). A parabolic mirror M focuses the diffracted beams on the respective exit slits. To reduce the aberrations in the water channel, the mirror is in a close to on-axis configuration for the water vapor wavelength. All slits have width of 1 mm and height of 8 mm and match the images of the entrance slit. The image width at the water vapor wavelength was found to be 0.93 mm only if the optical magnification of 2.7 (collimator and mirror), and the angular grating magnification of 1.73 are taken into account and increases to approximately 1 mm if the aberrations are considered. The bandwidth of the spectral transmission function was found to be around 0.33 nm if calculated using the reverse linear dispersion of the polychromator (about

0.3 nm mm^{-1} at the water vapor wavelength). The more precise ray-tracing calculation (OLSO®), which takes into account the system aberrations, confirmed this value. The calculated spectral transmission function for water vapor is presented in Fig. 10.

The total efficiency of the lidar receiver is defined generally by the polychromator transmittance and the PMT efficiency. To reduce the polychromator losses we use AR coated lenses and a dielectric mirror coating. The polychromator transmission, however, is defined mostly by the grating efficiency. We measured 36 % absolute grating efficiency (deviation angle of 26.3°) at the water vapor wavelength, a slightly reduced value compared to the specified by the producer 38 % efficiency in an auto-collimation configuration. The total polychromator transmittance at the water vapor wavelength becomes 33 % when the losses due to the coatings and the internal transmittance of the collimator optics are taken into account.

The polychromator rejection of the elastic stray light in the water vapor channel was measured by a stack of calibrated neutral density filters and was found to be 7×10^5. The elastic stray-light suppression of the channel is further enhanced by Semrock® Rasor edge filters installed in front of each fiber (in the telescope assembly) and at the polychromator entrance. Since the filters rejection at 355 nm is 10^6, the total rejection of elastic light in the water channel is estimated to be of 10^{17}. The cross-talk between the nitrogen and water vapor channels was measured using calibrated neutral density filters and the first nitrogen Stokes, produced by stimulated Raman scattering. The value of the cross talk was found to be 0.5×10^{-5}, low enough to be neglected as a cause of systematic errors even in the high troposphere.

An additional oxygen channel for determining the aerosol extinction correction of the water vapor concentration (Dinoev, 2003) was built, but is still not in use. Introducing of a third signal (oxygen) allows more precise correction for aerosol differential extinction but also introduces additional noise. Therefore, its use is justified only in a case of serious aerosol perturbation. More detailed investigation on the use of this correction is planned in near future.

As described in Part 2, the optics between the telescope and the photomultipliers can cause range dependence. To eliminate or reduce this range dependence to negligible levels we use a grating polychromator, fiber-coupled to the telescope assembly. Fiber coupling is essential for the elimination of C_L range-dependence since fibers perform aperture scrambling and fix the object position and size at the polychromator entrance, making it independent of the position and size of the image of the laser beam at the telescopes output. Furthermore, fiber coupling not only simplifies the lidar design and alignment, but also improves the system alignment stability compared to a free-space connection. Since the optical fibers do not perform complete angular scrambling, the angle of the light cone at the fibers exit depends on the observation range. This dependence is noticeable at distances shorter than 1 km and, combined with the polychromator aberrations, could lead to a range dependent error. To estimate the magnitude of this error, we used a ray-tracing model of the polychromator. The simulation showed maximum relative errors in the water vapor mixing ratio between −0.4 % and +0.1 % for the distance range 50–600 m. To avoid errors due to vigneting of the optical beams inside the polychromator, all the optical elements, including the grating, are oversized. To cancel the known effect of the PMT high spatial non-uniformity, we use Fourier lenses at the output of the polychromator, which convert the image of the input fiber slit (formed by five fibers) to single spots on the PMTs surfaces.

3.2.4 Light detection and signal acquisition

Hamamtsu metal channel dynode photomultipliers (PMT) are used for detecting the light in the Raman channels. This type of photomultipliers has been chosen because they show good counting characteristics and can be operated in both analog and photoncounting mode. Furthermore, their small size allows installation at the polychromator output without additional steering optics. To enhance the detection efficiency of the water vapor channel, we use high quantum efficiency (QE) photomultiplier (R7600U-200). The photocathode of this PMT is ultra-bialkali with 40 % quantum efficiency at 400 nm. The nitrogen and the oxygen channels are equipped with

Hamamatsu photodetector modules type H6780 with maximum quantum efficiency of 20 % at 400 nm. In order to preserve the photodetector modules from the high amplitude of the signals, and to use photon-counting mode, OD 1 and OD 0.6 neutral density filters are installed in the nitrogen and the oxygen channels, respectively.

During the four years of operation of the lidar we noticed a slight, steady decrease in the measured water vapor mixing ratio compared to the regular radiosonding. The decrease is more pronounced during the summer months, as shown in details in the companion paper (Broccard, 2012), and requires periodic lidar recalibration. Analyzing the possible reasons for this decrease we concluded that reduction of the photocathode sensitivity due to aging of the water vapor PMT is the most probable cause. Since the ultra-bialkali photocathodes are relatively new, there is no information about their aging. To monitor the absolute change in sensitivity of the water vapor PMT and its relative change versus the nitrogen PMT, we are developing a LED based monitoring system. The system will operate during standby periods of the lidar (rain, low clouds) and the information will be used for automatic correction of the lidar calibration constant and as an indication for PMT exchange.

Data acquisition is carried out by a Licel GmbH transient recorder having simultaneously operated 250 MHz counter and a 12 bit, 40 MSPS analog digitizer. The minimum time resolution is 25 ns corresponding to a 3.75 m spatial resolution. The transient recorder channels are synchronously triggered by an optical trigger activated by the 532 nm laser radiation. Optical triggering eliminates the electric connection between the laser and the transient recorder, thus reducing any possible electromagnetic interference. The raw signals are acquired in analog-to-digital (AD) and photon-counting (PhC) modes with spatial resolution of 3.75 m and temporal averaging over 1800 laser shots (approximately one minute).

3.2.5   Lidar automation

The lidar autonomous operation is ensured by two computers. The first one, a lidar automat computer (LAC), controls the lidar hardware, records the hardware operational

Title Page

Abstract   Introduction

Conclusions   References

Tables   Figures

|◄   ►|

◄   ►

Back   Close

Full Screen / Esc

Printer-friendly Version

Interactive Discussion

parameters and acquires the raw lidar data. A second, data treatment computer (DTC), is designated for automated, onsite data treatment and data transfer.

A lidar automat (LA) code that runs in LabView environment on LAC controls the lidar and can be operated in Auto or Manual modes. In the Auto mode, the lidar operates autonomously after initial activation by the operator. In this mode LAC controls the lidar hardware and terminates and resumes the measurements depending on the weather conditions. Weather information is supplied by a precipitation detector, and a collocated ceilometer. The program stops the lidar in case of precipitation, clouds lower than 500 m, or dense fog and restarts it when the cloud base is higher than 1.5 km and if no rain or fog are detected within predefined time interval. After initial timeout for the laser heat-up, the acquisition system is activated and the lidar is operational. The laser power is continuously monitored and an automated alignment of the harmonic crystals is activated when the power at 355 nm drops below a predefined level. All metadata, relevant to the lidar, including the laser power is logged. In manual mode, the automated procedures for lidar startup, operation, and stop are deactivated, leaving the control to the operator.

The real-time data treatment is performed by an automated data treatment (ADT) program, developed under Matlab and run on the DTC. Each half an hour the program reads the available raw data files, processes the data, and stores the result in a file available for upload. The file consists of a water vapor mixing ratio profile with the corresponding statistical error. Remote control of the system is available via secured internet connection.

4   Data treatment

The data treatment software was designed to autonomously process the raw data in near-to-real time and to transfer the water vapor mixing ratio profile and its relative error estimate to the MeteoSwiss data base. The data treatment procedure is carried out every half an hour when data are available

4.1 Profile retrieval

The profile retrieval consists of the following steps: desaturation of the PhC signals and scaling the AD water vapor signal to PhC; calculation of the signal and background variance from Poisson statistics; background subtraction; time and space averaging; water vapor mixing ratio calculation using predefined calibration constant; Rayleigh correction. The PhC signals from all detection channels are desaturated using the assumption for "non-paralyzable" counter (Ingle, 1972)

$$P_i^d = \frac{P_i}{(1 - \tau P_i)} \tag{8}$$

where P_i^d is the desaturated count rate from a distance bin i, P_i is the measured count rate and τ is the counter dead time. Since some of the daytime water signals are oversaturated, we use glued water signals consisting of PhC and scaled AD signals for the processing. The AD signal is scaled to match the PhC signal according to the following formula:

$$P_i^{AS} = \frac{S_i^A - u_0}{C} \tag{9}$$

where P_i^{AS} is scaled analog signal S_i^A, C is scaling coefficient and u_0 is the electric offset of the ADC. The dead time and the scaling coefficient are calculated by a linear regression of PhC to AD signals and the electric offset is derived from the last 1000 bins of night-time acquired AD signals. The glued signal is equal to P_i^{AS} for photon count rates above a predefined threshold, and equal to P_i^d for photon count rates below this threshold. The signal noise is calculated before the background subtraction, using either a signal variance from Poisson statistics, or a variance estimate from a digitized analog signal (Liu, 2006). The background value in each channel is determined from the last 1000 time bins. The corrected signals are averaged over 30 min. The spatial

averaging is done using a window size, which is variable as a function of height. The window size is defined by the software to maintain the relative error below 10 %. The relative error is calculated using Eq. (9). The water vapor mixing ratio is derived from the ratio of water vapor to nitrogen Raman signals following Eq. (3), where the calibration
5 constant is obtained from a set of inter-comparisons with radiosondes. Finally the water vapor profile is corrected for molecular atmospheric differential transmission using US standard atmosphere model.

4.2 Error calculations

The measurement error of the water vapor profile has three main components (White-
10 man, 2003): uncertainty of the calibration constant, uncertainty in the differential atmospheric extinction, and most importantly, random error of water vapor to nitrogen signal ratio.

The uncertainty of the calibration constant is mostly systematic and due to the uncertainty of the reference instrument and the calibration methodology, but it also depends
15 on the temperature sensitivity of the Raman signals. All of these components can be kept low through proper reference instrument selection and calibration procedure and through the lidar's design.

The uncertainty of the differential atmospheric transmission arises both through Rayleigh and aerosol scattering, but is relatively low in conditions of normal visibility.
20 The dominating error source of the water vapor measurement is the statistical error of the lidar signals due to photon detection noise. The statistics of the signals detected in photon-counting mode is governed by the Poisson distribution i.e. the standard error is equal to the square root of the number of photons counted. The relative error $\frac{\partial q(z)}{q(z)}$

of the water vapor measurement is estimated from the standard errors of the Raman signals $\sigma_x(z)$ and their respective daytime background $\sigma_{Bx}(z)$ as:

$$\frac{\partial q(z)}{q(z)} = \sqrt{\frac{\sigma_{H_2O}^2(z) + \sigma_{BH_2O}^2}{[N_{H_2O}(z) - N_{BH_2O}]^2} + \frac{\sigma_{N_2}^2(z) + \sigma_{BN_2}^2}{[N_{N_2}(z) - N_{BN_2}]^2}} \tag{10}$$

where N_x is the number of the signal counts summed over the averaging time and space range and N_{Bx} is the number of the respective background counts.

The absolute error of the lidar water vapor profile was estimated by comparison of one year humidity measurements simultaneously taken by the lidar, collocated regular radiosonding, a microwave radiometer, and a GPS receiver. The results of this inter-comparison are discussed in the companion paper (Broccard, 2012) and show good agreement of the three measurement techniques. This agreement signifies that the absolute error of the lidar profiles is at least within the uncertainty of the mentioned conventional techniques.

5   Measurement examples

Figure 11 shows night-time recorded nitrogen and water vapor desaturated photon counting signals, summed over 5 min (9×10^3 laser shots) using 37.5 m (10 bin) vertical resolution, presented in a count rate (MHz) and photon counts. The desaturated nitrogen signal has a maximum value of 110 MHz, whereas the water vapor signal, recorded in relatively dry night-time conditions, reaches 17 MHz. The first peak in Raman signals at approximately 0.7 km clearly shows an increase in the collection efficiency due to the NR fiber. The second peak, at approximately 1.3 km, is due to signal collection by the primary fibers in the four telescopes.

The lidar calibration constant is derived using vertical profiles taken by either Vaisala RS-92 or Snow White (Vömel, 2003) radiosondes. The calibration flights were carried out in night-time and stable weather conditions. The Snow-White dew point profile is

converted to mixing ratio with Goff-Gratch equations for saturation pressure over water and ice (1946 formulation), accounting for the internal flag indicating ice formation on the mirror. The same calibration constant is used for several months and is periodically verified. Recalibration is done when the calibration error exceeds a predefined level.

5   The calibration constant used in the following examples was derived from a Vaisala RS 92 profile using the first 6 km of the profile.

Figure 12 shows comparison of night time water vapor mixing profiles obtained by the lidar and a Snow-White radiosonde, launched from the lidar site on 26 August 2008 at 19:38 UTC. The left plot presents comparison of the mixing ratio profiles, and the right

10 plot shows the statistical error profile of the lidar measurement. Mixing ratios higher than $2\,g\,kg^{-1}$ are presented in a linear scale, whereas the smaller values are plotted in a logarithmic scale. The linear scale compares the data up to approximately 3 km, an altitude reached by the radiosonde for about 10 min, assuming radiosonde ascending rate of about $5\,m\,s^{-1}$. For better comparison with the sonde profile, the lidar data was

15 averaged for 10 min within the first 3 km. The logarithmic scale compares the lidar and the radiosonde using a lidar mixing ratio profile obtained with 30 min time average. The vertical resolution of the lidar is variable in order to keep the statistical error below 10 %. The initial resolution is 15 m, it is reduced to 30 m above 4 km, to 105 m above 6.5 km, and to 300 m above 9 km. Above 11 km the range resolution is 900 m. Error

20 bars at the beginning and the end of the lidar profile present the statistical error of the lidar measurement, estimated from the lidar signals.

The mixing ratio profiles match exceptionally well within the whole range from 75 m up to 12.5 km. The very good agreement in the lower parts of the profiles, retrieved from the incomplete overlap region, demonstrate the negligible range dependence of

25 the lidar calibration constant. The small discrepancies between the sonde and the lidar, seen in the lower part of the profile, can be explained by the different temporal and spatial resolutions of the two instruments, amplified by the high temporal and spatial variability of the water vapor field. The validity of the last argument is supported by the high temporal variability of the water vapor field clearly seen in the 10 min resolution

Back | Close

Full Screen / Esc

Printer-friendly Version

Interactive Discussion

time series presented in Fig. 14. The lidar correctly reproduces the atmospheric stratification observed by the radiosonde. The differences between the sonde and the lidar in the 5–5.5 km region are probably caused by the difference in the air masses sampled by the two instruments, or by the smoothing effect of the longer time averaging by the lidar, or both.

The two profiles compare very well in the region 6.5–11 km, despite the reduced to 105 m lidar resolution. The very good correlation in this region is an indicator for the negligible temperature sensitivity of the measurements i.e. the correct selection of polychromator central wavelengths and bandwidths. Above 11 km the relative error increases above 10 % and to compensate, the software increases the vertical averaging to 900 m, defining a measurement point at 11.8 km (relative error 19 %), followed by a measurement point at 12.6 km (relative error of ∼ 40 %). Above that altitude the noise prevails. It is worth to mention that the laser is operated at 9 W. Increasing the power to its nominal 12 W value and longer averaging time could extend the measurements into the lower stratosphere when necessary.

Daytime lidar mixing ratio profile obtained on 9 April 2009 is shown in Fig. 13. The lidar data is averaged from 11:00 to 11:30 UTC with initial vertical averaging of 30 m, increased to 75 m at 2.5 km, and to 300 m above 4 km. The profile is compared to an equipped with Vaisala RS 92 radiosonde, launched at 11:00 UTC (13:00 local time). The right plot shows the relative error profile of the lidar measurement derived from the signal statistics. The first lidar point is at 75 m, and the measurement statistical error is about 5 % due to the sky background in the water vapor channel. A well-mixed boundary layer defines an almost constant mixing ratio profile up to about 700 m, captured by both instruments without big differences. Within the range from 700 to about 1.6 km, the mixing ratio decreases to about $1.5 \, \mathrm{g \, kg^{-1}}$. Small difference between the profiles is present and could be explained by variation of the water vapor field, which is typical for daytime conditions with strong vertical mixing. At above 1.6 km the lidar signal amplitude decreases (due to z^{-2}) and the statistical error increases despite the almost constant up to 2.5 km mixing ratio. Compared to night time measurements the

Title Page

Abstract | Introduction

Conclusions | References

Tables | Figures

|◀ | ▶|

◀ | ▶

Back | Close

Full Screen / Esc

Printer-friendly Version

Interactive Discussion

statistical error is higher mainly due to the presence of daytime sky background in the water vapor channel.

In order to explore the full potential of the lidar to resolve the spatio-temporal evolution of a water vapor field, time series with high temporal and spatial resolution were taken in favorable weather conditions while operating the laser at its nominal energy of 400 mJ (12 W). As already mentioned, during regular operations the laser output energy is limited to 300 mJ (9 W) to extend the life-time of the flash lamps and to prevent damage of the optical elements of the laser and the transmitter. The lidar performance at reduced energy is sufficient for regular profiling, as demonstrated by a companion paper (Broccard, this issue) and the lidar can always be operated at nominal laser energy in case of special events.

Figure 14 presents time series with high temporal and spatial resolution taken from 26 August to 1 September. The temporal resolution of the data is 10 min and the vertical resolution is 30 m up to 4 km, and 75 m above this height. The white strips indicate an absence of data. The high spatio-temporal resolution of the profiles allows visualizing well-known, but difficult to observe with the classical methods, processes, such as the enhanced turbulent mixing in the boundary layer during the early afternoon, seen as alternating red and orange vertical strips with changing intensity around 12:00 UTC. Another interesting atmospheric phenomenon, besides the temporal evolution of the boundary layer, is the subsidence of dry air from high altitudes to the lower troposphere. The most pronounced subsidence during the observational period was recorded on 28 August and is probably the result of stratosphere-troposphere exchange. The fast temporal evolution and spatial displacement of water vapor concentration as seen from Fig. 14 can explain a great part of the lidar to sonde discrepancies observed in the previous examples.

RALMO Part I: Instrument description

T. S. Dinoev et al.

Title Page

Abstract | Introduction

Conclusions | References

Tables | Figures

◀ | ▶

◁ | ▷

Back | Close

Full Screen / Esc

Printer-friendly Version

Interactive Discussion

6 Summary and outlook

A new Raman lidar designed for unattended, continuous measurement of vertical water vapor profiles for operational meteorology has been described. To attain daytime operation, the lidar uses narrow-field-of-view (NFOV), narrow-band (NB) configuration and a 15× beam expander ensures low beam divergence, essential for the NFOV design, and reduces the laser energy density to levels meeting eye safety regulations. The receiver consists of four 30 cm in diameter mirrors fiber-coupled to a grating polychromator. The detection is carried out by Hamamatsu metal dynode photomultipliers and a Licel transient recorder acquires the signals in analog and photoncounting mode. The need for range-dependent overlap corrections is eliminated by the careful design of the receiver, which eliminates the range dependence of the instrumental part of the lidar calibration constant, thus allowing data retrieval from the incomplete overlap region without the need for range (overlap) corrections. Additional fiber in one of the telescope mirrors collects the scattered light from the near-range, thus extending the distance range down to 100 m. The value of the temperature correction is reduced to levels around 1 % by selection of the polychromator central wavelength and bandwidth. The opto-mechanical design of the lidar ensures long-term alignment stability and eliminates the need for frequent transmitter-receiver alignments. The unattended automated control of the lidar is carried out by two computes controlling the hardware and performing automated data treatment. After its installation in July 2007 and the initial tests, the lidar has been in regular operation since August 2008 at the main aerological station of the Swiss Meteorological Office (MeteoSwiss).

Since 2007 the lidar has shown annual technical availability between 65 and 90 %. More information on this is available in the companion paper (Broccard, this issue). The main technical problems encountered during the first three years of operation were related to the laser or the supporting equipment (cooling water chiller, air conditioning, roof hatch). The technical unavailability due to the supporting equipment and some of the laser problems, namely those related to the internal cooling system, were resolved

to a great extent. A persisting problem is the laser misalignment after flash-lamp re-placement, caused by insufficient positioning accuracy of the oscillator and amplifier pumping chambers. Redesigning of the pumping chambers and their support, planned in the near future, is expected to resolve this problem.

The lidar was upgraded with a pure rotational Raman channel for temperature, aerosol backscatter and extinction measurements, which is operational in test mode since 2009. The channel design and analysis of the data will be presented in a sepa-rated paper after completing the test period and starting regular operations.

References

Ansmann, A., Riebesell, M., Wandinger, U., Weitkamp, C., Voss, E., Lahmann, W., and Michaelis, W.: Combined Raman elastic-backscatter LIDAR for vertical profiling of moisture, aerosol extinction, backscatter, and LIDAR Ratio, Appl. Phys. B, 42, 18–28, 1992.

Apituley, A., Wilson, K., Potma, C., Volten, H., and de Graaf, M.: Performance assessment and application of CAELI – A high-performance Raman lidar for diurnal profiling of Water Vapour, Aerosols and Clouds, Proceedings of the 8th International Symposium on Tropospheric Pro-filing, ISBN 978-90-6960-233-2 Delft, The Netherlands, October 2009, edited by: Apituley, A., Russchenberg, H. W. J., and Monna, W. A. A., S06-O10, 2009.

Arnold, D. L.: Severe deep moist convective storms: Forecasting and mitigation, Geography Compass, 2, 30–66, 2008.

Avila, G., Fernandez, J. M., Mate, B., Tejeda, G., and Montero, S.: Ro-vibrational Raman cross sections of water vapor in the OH stretching region, J. Mol. Spec., 196, 77–92, 1999.

Balin, I., Serikov, I., Bobrovnikov, S., Simeonov, V., Calpini, B., Arshynov, Y., and and van den Bergh, H.: Simultaneous measurement of atmospheric temperature, humidity, and aerosol extinction and backscatter coefficients by a combined vibrational-pure-rotational Raman lidar, Appl. Phys. B, 79, 775–782, 2004.

Bösenberg, J. and Linné, H.: "Continuous ground-based water vapor profiling using DIAL, Reviewed and revised papers presented at 23rd ILRC, 24–28 July 2006, Nara Japan, 679–683, 2006.

Broccard, E., Philippona, R., Haefele, A., Romanens, G., Ruffieux, D., Simeonov, V., and Calpini, B.: Raman Lidar for Meteorological Observations, RALMO – Part 2: Validation of water vapor measurements, Atmos. Meas. Tech. Discuss., 5, 6915–6948, doi:10.5194/amtd-5-6915-2012, 2012

Browell, E., Ismail, S., and Grant, W.: Differential absorption lidar (DIAL) measurements from air and space, Appl. Phys. B, 67, 399–410, 1998.

Bruneau, D., Quaglia, P., Flamant, C., Meissonnier, M., and Pelon, J.: Airborne Lidar LEANDRE II for Water-Vapor Profiling in the Troposphere. I. System description, Appl. Opt., 40, 3450–3461, 2001.

Cooney, J.: Remote measurements of atmospheric water vapor profiles using the Raman component of laser backscatter, J. Appl. Meteorol., 9, 182–184, 1970.

Cooney, J., Petri, K., and Salik, A.: Measurements of high resolution atmospheric water vapor profiles by use of a solar blind Raman lidar, Appl. Opt., 24, 104–108, 1985.

Dinoev, T., Arshinov, Y., Bobrovnikov, S., Serikov, I., Calpini, B., van den Bergh, H., and Simeonov, V.: Meteorological water vapor Raman lidar – advances, Reviewed and revised papers presented at 23rd ILRC, 24–28 July 2006, Nara Japan, 47–49, 2006.

Engelbart, D., Reichardt, J., Mattis, I., Wandinger, U., Klein, V., Meister, A., Hilber, B., and Jaenisch, V.: RAMSES – German meteorological service Raman lidar for atmospheric moisture measuring, Reviewed and revised papers presented at 23rd ILRC, 24–28 July 2006, Nara Japan, 683–686, 2006.

Goldsmith, J., Blair, F. H., Bisson, S. E., and Turner, D. D.: Turn-key Raman lidar for profiling atmospheric water vapor, clouds, and aerosols, Appl. Opt., 37, 4979–4990, 1998.

Ingle, J. D. and Crouch, S.: Pulse overlap effects on linearity and signal-to-noise ratio in photon counting systems, Anal. Chem., 4, 777–784, 1972.

Liu, Z., Hunt, W., Vaughan, M., Hostetler, C., McGill, M., Powell, K., Winker, D., and Hu, Y.: Estimating random errors due to shot noise in backscatter lidar observations, Appl. Opt., 45, 4437–4447, 2006.

Measures, R. M.: Laser remote sensing: fundamentals and applications, Krieger publishing company, Florida, p. 225, 1992.

Melfi, S. H.: Remote Measurements of the Atmosphere Using Raman Scattering, Appl. Opt., 11, 1605–1610, 1972.

Nash, J., Oakley, T., Vomel, H., and Wei, L.: WMO intercomparison of high quality radiosonde systems, Yangjiang, China, 12 July–3 August 2010, Tech. Rep. 107, World Meteorological Organization, WMO/TDNo.1580, 2011.

Normand, C. W.: On instability from water vapour, Q. J. Roy. Meteorol. Soc., 64, 47–70, 1938.

Peppler, R. A.: Tropospheric Static Stability and Central North American Growing Season Rainfall, Mon. Weather Rev., 117, 1156–1180, 1989.

Renaut, D., Pourny, J., and Capitini, R.: Daytime Raman-lidar measurements of water vapor, Opt. Lett., 5, 233–235, 1980.

Schneider, M. and Hase, F.: Ground-based FTIR water vapour profile analyses, Atmos. Meas. Tech., 2, 609–619, doi:10.5194/amt-2-609-2009, 2009.

Sherlock, V., Garnier, A., Hauchecorne, A., and Keckhut, P.: Implementation and validation of a Raman lidar measurement of middle and upper tropospheric water vapor, Appl. Opt., 38, 5838–5850, 1999.

Simeonov, V., Larcheveque, G., Quaglia, P., van den Bergh, H., and Calpini, B.: Influence of the photomultiplier tube spatial uniformity on lidar signals, Appl. Opt., 38, 5186–5190, 1999.

Simeonov, V., Dinoev, T., Calpini, B., Bobrovnikov, S., Arshinov, Y., Ristori, P., van den Bergh, H., and Parlange, M.: A Raman lidar as operational tool for water vapor profiling in the Swiss meteorological office, ILRC 25 St. Petersburg, 1175–1178, 2010

Sinha, A.: Water vapour and greenhouse trapping: The role of far infrared absorption, Geophys. Res. Lett., 22, 2147–2150, 1995.

Solheim, F.: Radiometric profiling of temperature, water vapor and cloud liquid water using various inversion methods, Radio Sci., 33, 393–404, 1998.

Vaughan, G. Wareing, D. P., Thomas, L., and Mitev, V.: Humidity measurements in the free troposphere using Raman backscatter, Q. J. Roy. Meteorol. Soc., 114, 1471–1484, 1988.

Vömel, H., Fujiwara, M., Shiotani, M., Hasebe, F., Oltmans, S. J., and Barnes, J. E.: The behavior of the Snow White chilled-mirror hygrometer in extremely dry conditions , J. Atmos. Ocean. Tech., 20, 1560–1567, 2003.

Whiteman, D. N.: Raman lidar system for the measurement of water vapor and aerosols in the Earth's atmosphere, Appl. Opt., 31, 3068–3082, 1992.

Whiteman, D. N.: Examination of the traditional Raman lidar technique. I. Evaluating the temperature-dependent lidar equations, Appl. Opt., 42, 2571–2592, 2003.

RALMO Part I: Instrument description

T. S. Dinoev et al.

Title Page

Abstract | Introduction

Conclusions | References
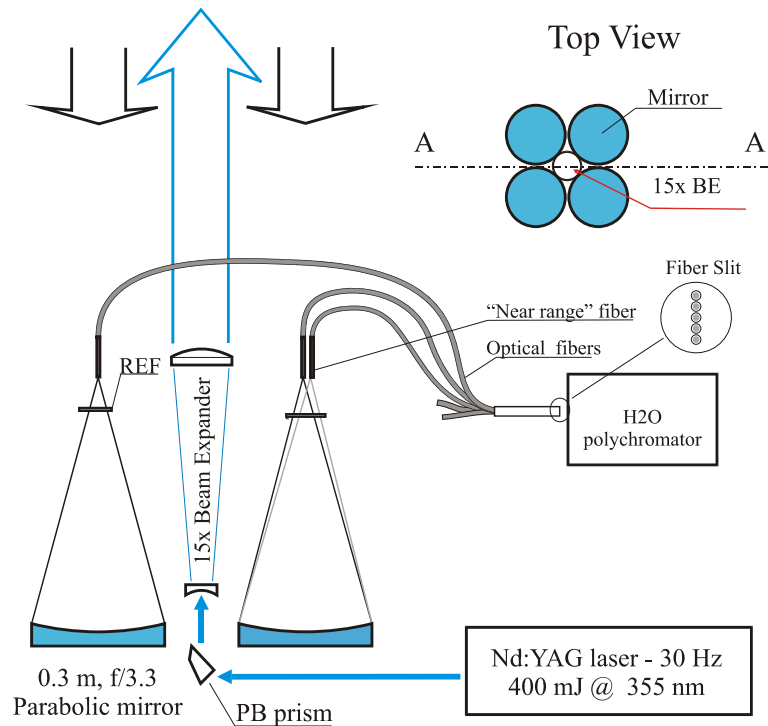
Tables | Figures

|◄ | ►|

◄ | ►

Back | Close

Full Screen / Esc

Printer-friendly Version

Interactive Discussion

Whiteman, D. N., Cadirola, M., Venable, D., Calhoun, M., Miloshevich, L., Vermeesch, K., Twigg, L., Dirisu, A., Hurst, D., Hall, E., Jordan, A., and Vömel, H.: Correction technique for raman water vapor lidar signal dependent bias and suitability for water vapor trend monitoring in the upper troposphere, Atmos. Meas. Tech. Discuss., 4, 7337–7403, doi:10.5194/amtd-4-7337-2011, 2011.

Wirth, M., Fix, A., Mahnke, P., Schwarzer, H., Schrandt, F., and Ehret, G.: The airborne multi-wavelength water vapor differential absorption lidar WALES: system design and performance, Appl. Phys. B, 96, 201–213, 2009.

Wulfmeyer, V. and Bosenberg, J.: Ground-based differential absorption lidar for water-vapor profiling: assessment of accuracy, resolution, and meteorological applications, Appl. Opt., 37, 3825–3844, 1998.

Wulfmeyer, V., Behrendt, A., Bauer, H., Kottmeier, C., Corsmeier, U., Blyth, A., Craig, G., Schumann, U., Hagen, M., Crewell, S., Di Girolamo, P., Flamant, C., Miller, M., Montani, A., Mobbs, S., Richard, E., Rotach, M., Arpagaus, M., Russchenberg, H., Schlüssel, P., König, M., Gärtner, V., Steinacker, R., Dorninger, M., Turner, D., Weckwerth, T., Hense, A., and Simmer, C.: The Convective and Orographically Induced Precipitation Study, B. Am. Meteorol. Soc., 89, 1477–1486, 2008.

Table 1. System parameters.

Transmitter		Receiver	
Nd:YAG laser:		Four parabolic mirrors:	
Wavelength:	354.7 nm	Focal length:	1 m
Spectral line width:	0.7 cm^{-1}	Diameter:	0.3 m
Rep. rate:	30 Hz	Total aperture:	2827.4 cm^2
Pulse energy:	300 mJ	Axial displacement:	235 mm (to expander axis)
Pulse duration:	8 ns	FOV:	3×0.20 and 1×0.22 mrad
Transmitted beam:		Polychromator:	
Divergence:		Bandwidth (FWHM):	0.33 nm (H_2O and N_2)
calculated	0.06 mrad	Efficiency:	33 % (peak at H_2O)
measured	0.09 ± 0.02 mrad		
Diameter:	140 mm		

Fig. 1. Lidar optical scheme: A 15× beam expander is centered in-between four 30 cm in diameter, f/3.33 parabolic mirrors as illustrated by the top view shown in the upper right corner. The optical scheme is a cross section along the line A-A of the top view, therefore only two of the telescope mirrors can be seen; REF – Razor edge filter (Semrock®); PB – Pellin–Broca prism; PMT – photomultiplier.

Full Screen / Esc

Printer-friendly Version

Interactive Discussion
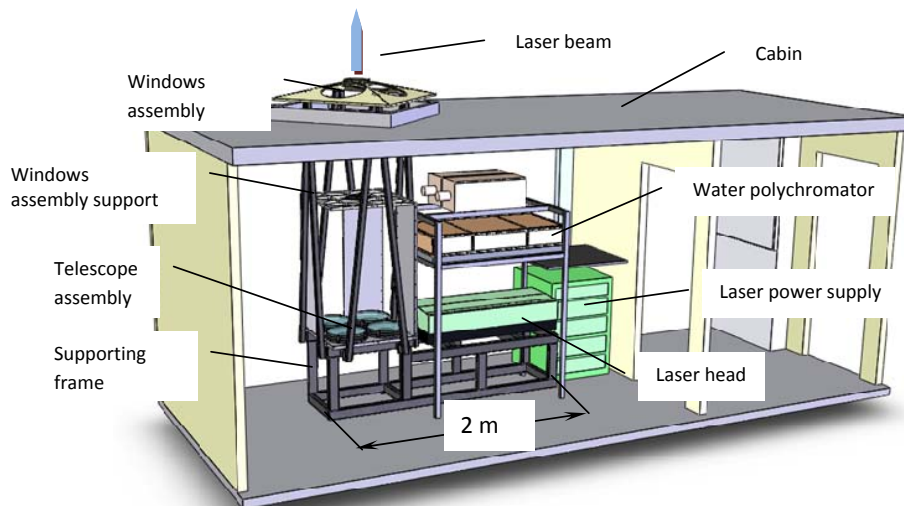
Fig. 2. Mechanical setup of the lidar; a support frame welded from square stainless steel tubing holds the telescope assembly, the laser head, and a protective window support; the lidar polychromator is mechanically separated from the telescopes using fiber coupling (not shown in the figure).
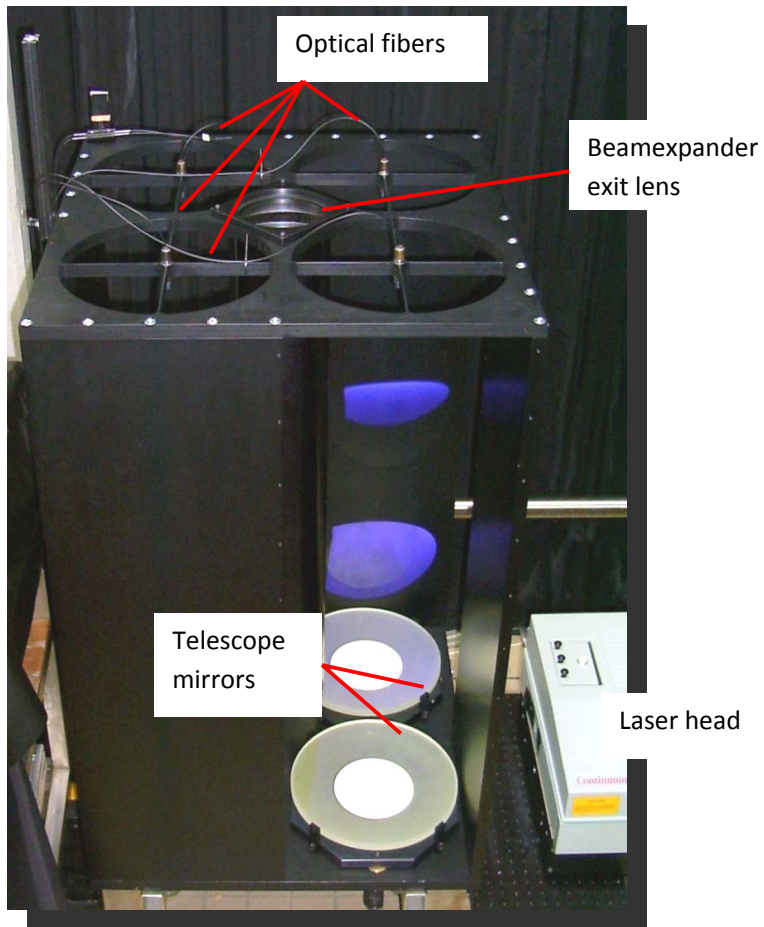
Fig. 3. Photograph of the telescope assembly taken before installation of the windows assembly support. Two of the four telescope mirrors are seen.
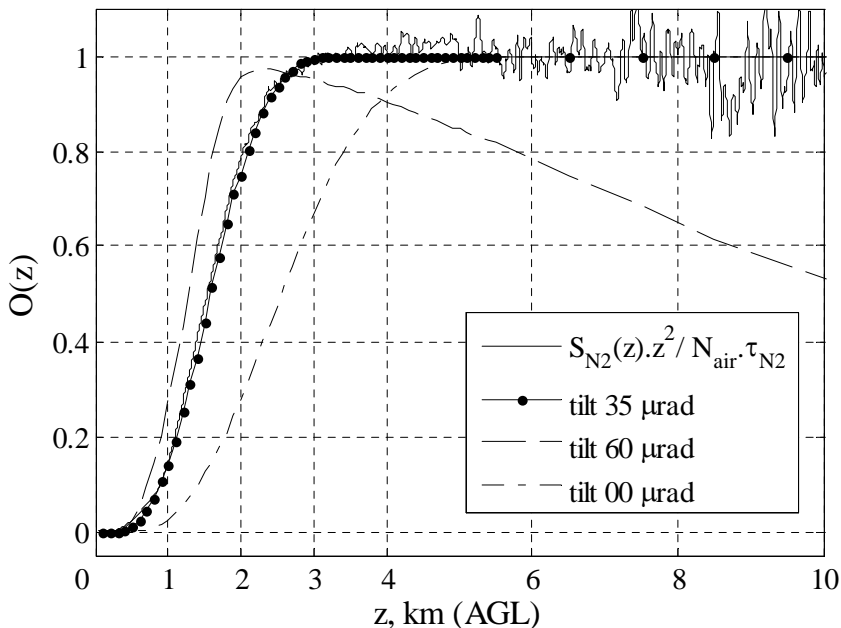
Fig. 4. Calculated overlap functions for different mirror tilt angles, compared to derived from acquired nitrogen signal overlap function. The overlap functions were calculated for the telescopes focused at 10 km (0.1 mm fiber shift away from the mirrors), whereas the overlap estimate uses nitrogen signal recorded on 9 July 2008, averaged for 1 min (1800 laser shots) and over 37.5 m (10 bins).

Title Page

Abstract | Introduction

Conclusions | References

Tables | Figures

|◄ | ►|

◄ | ►

Back | Close

Full Screen / Esc

Printer-friendly Version

Interactive Discussion
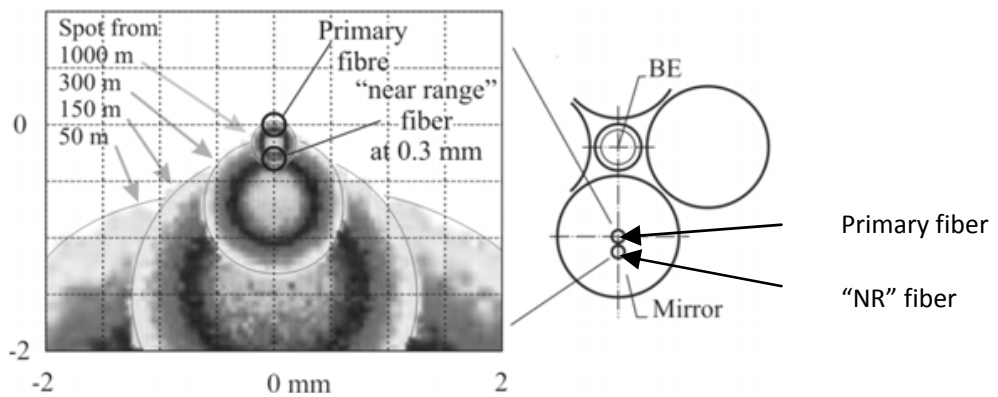
Fig. 5. Positions of the primary and NR fibers and the blur spot contours at the focal plane of a telescope mirror: left – modeled blur spot contours from different distances; right – a sketch of the receiver showing the positions of the primary and NR fibers, the beam expander (BE), and the telescope mirrors.
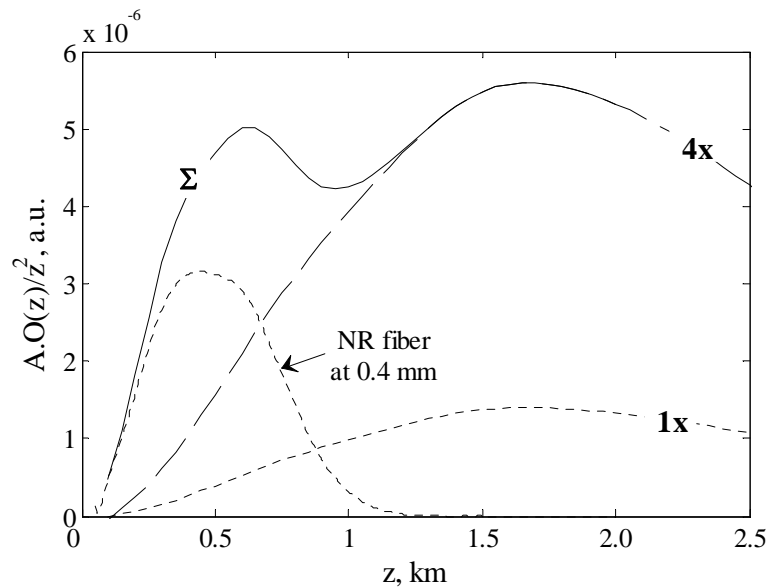
Fig. 6. Simulated signals in terms of $AO(z)/z^2$ disregarding the atmospheric transmission; signal from one telescope (1×), signal from four telescopes (4×), total signal from four telescopes including the contribution of the near range fiber (Σ).
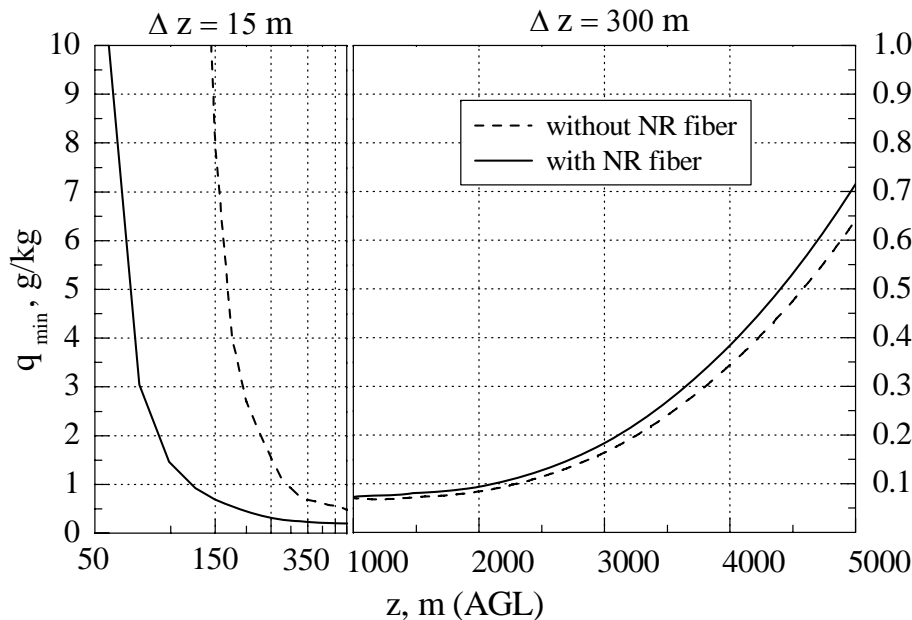
Fig. 7. NR fiber influence on the minimum detectable water vapor mixing ratio profiles (SNR = 10); averaging 30 min, 65 MHz sky background in the water vapor channel, molecular two-way attenuation from US standard atmosphere, aerosol two-way transmission assuming constant aerosol extinction at 550 nm of 0.11 up to 1.5 km with Angström coefficient of 1.4.
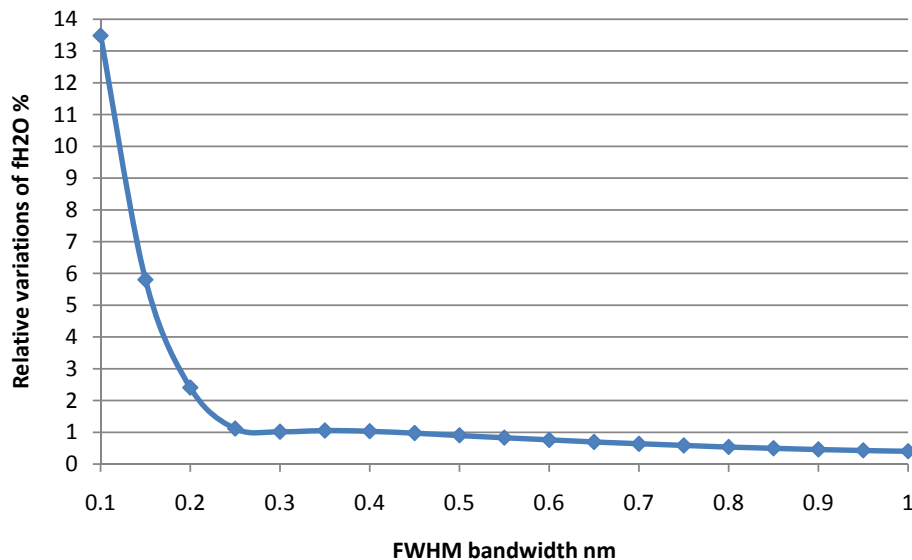
Fig. 8. Minimum values of the relative variations of as a function of the water vapor channel FWHM bandwidth for the temperature range-60 °C + 40 °C.
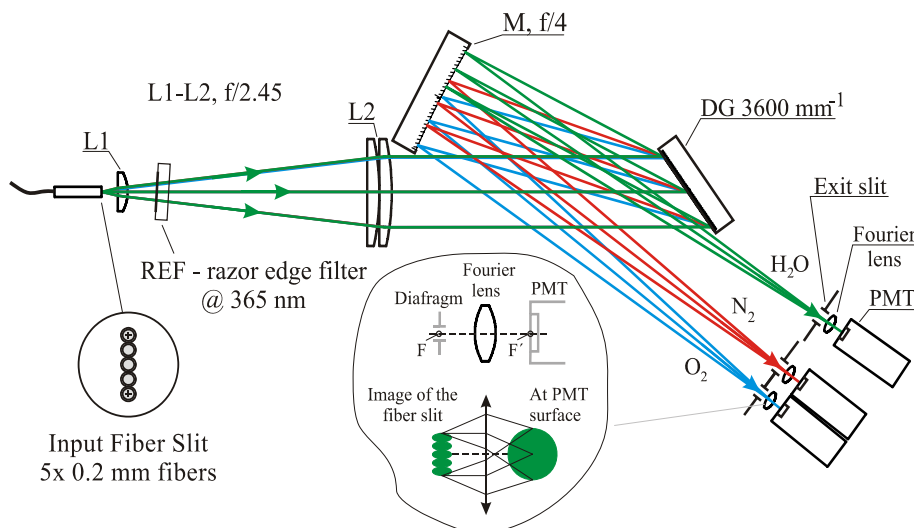
Fig. 9. Optical layout of the polychromator: L1 – L2 spherical lens collimator (f/2.39, $F = 165$ mm), REF – Raman edge filter, DG – holographic diffraction grating (3600 mm^{-1}, 85×85 mm^2), M – parabolic mirror (f/4, $F = 445$ mm), PMT photomultiplier tubes.
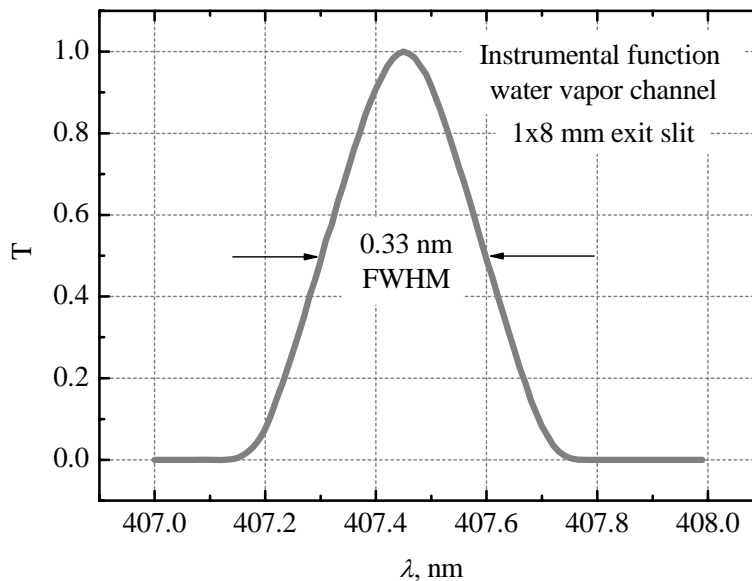
Fig. 10. Instrumental function of the water vapor channel calculated with OLSO® for exit slit width of 1 mm. The function maximum is centered at 407.45 nm for minimal temperature influence.
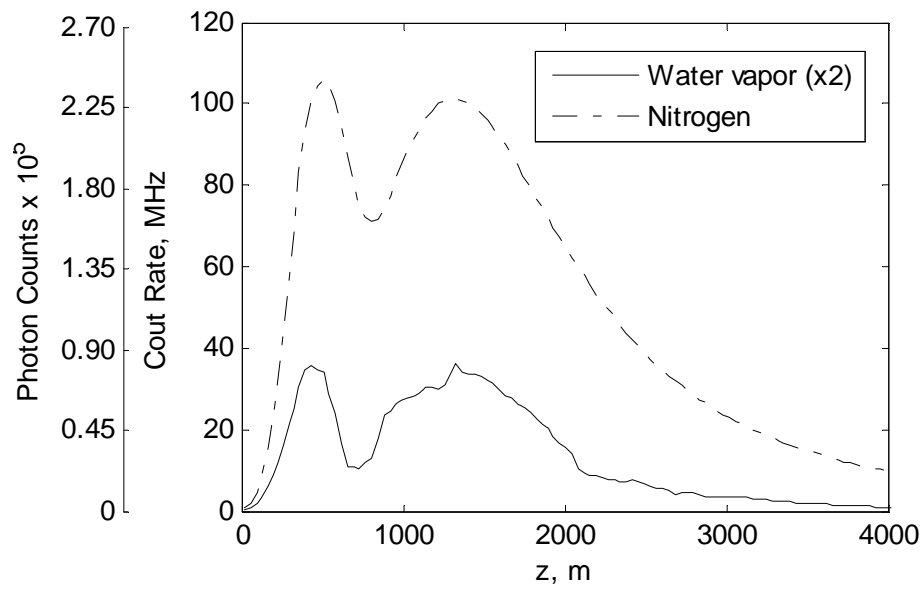
Fig. 11. Lidar signals from water vapor and nitrogen channels.
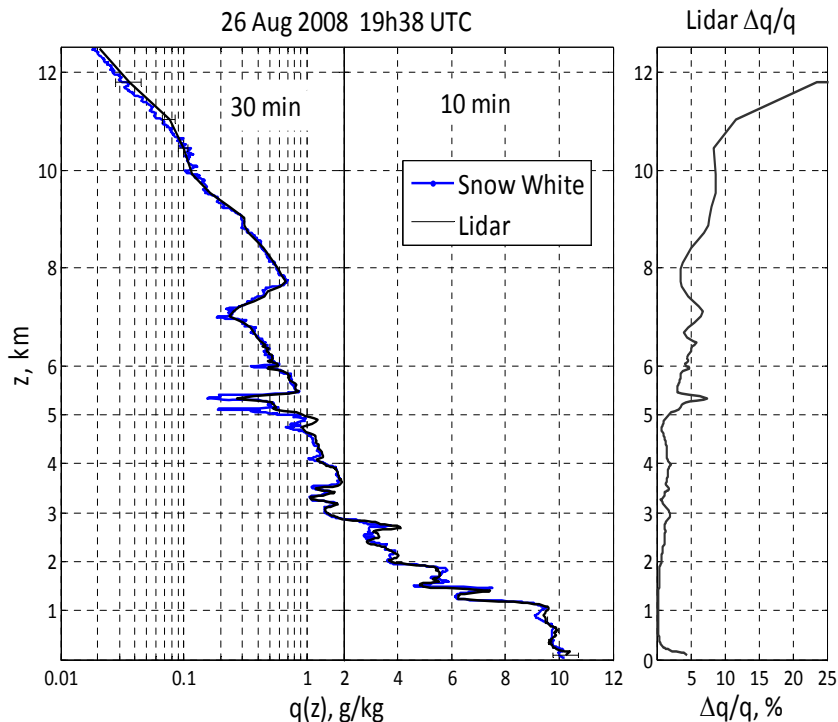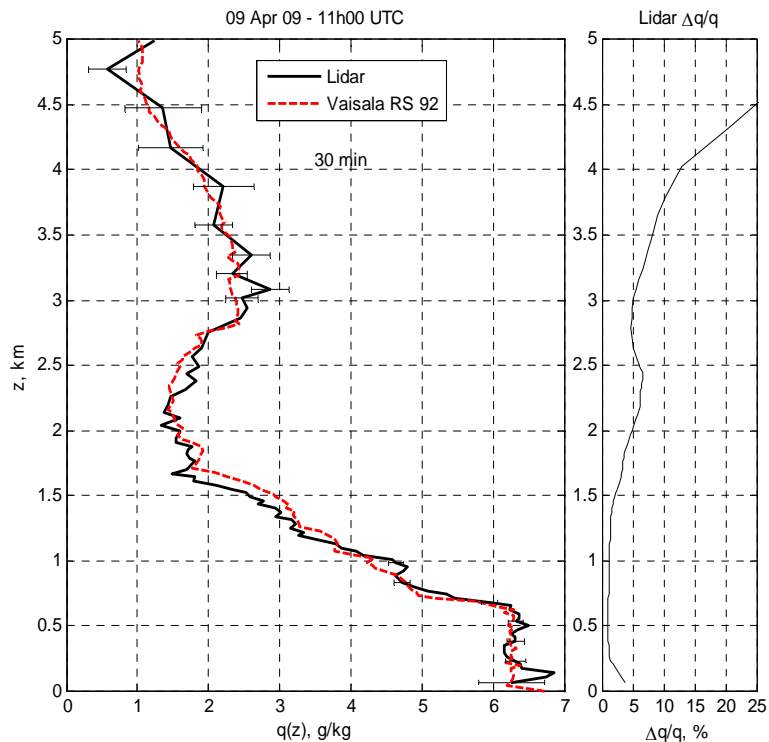
Fig. 12. Left – Vertical water vapor mixing ratio profiles measured quasi-simultaneously by the lidar and an equipped with Snow White radiosonde (chilled mirror hygrometer). The sonde was launched at 19:38 UTC. Time averaging 10 min below 3 km and 30 min above. The vertical resolution is variable; initial 15 m, above 4 km – minimum 30 m, above 6.5 km – minimum 105 m, above 9 km – minimum 300 m; above 11 km the resolution is 900 m (maximum allowed). Right Lidar statistical error profile.
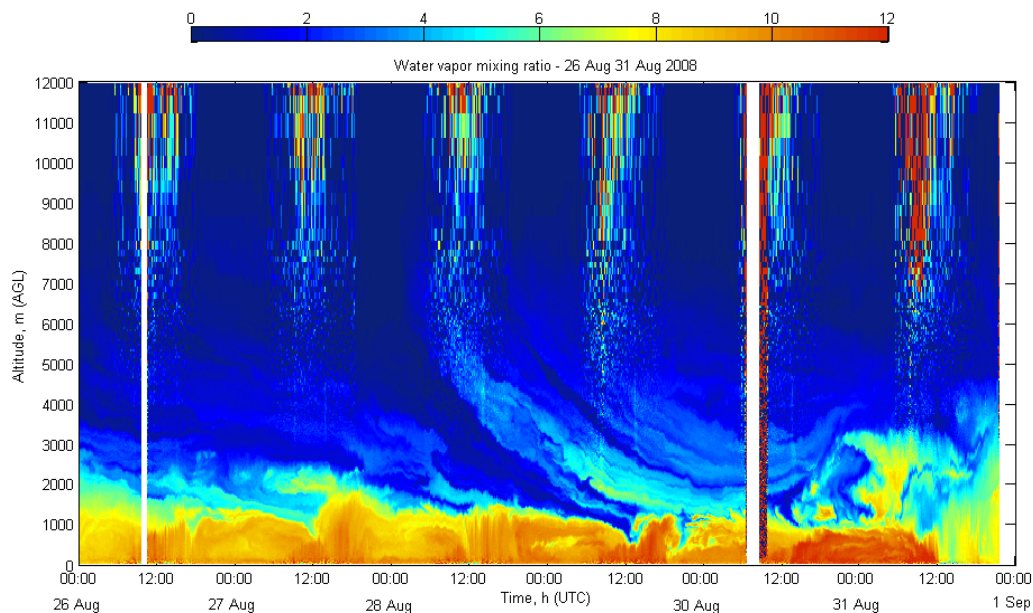
Fig. 13. Left Daytime profiles of water vapor mixing ratio compared to Vaisala RS-92 radiosonde launched on 9 April 2009 at 11:00 UTC; Right Lidar statistical error profile.

RALMO Part I: Instrument description

T. S. Dinoev et al.

Title Page

Abstract | Introduction

Conclusions | References

Tables | Figures

|◄ | ►|

◄ | ►

Back | Close

Full Screen / Esc

Printer-friendly Version

Interactive Discussion

Fig. 14. Six day time series of water vapor with 10 min time resolution. All data are shown, including data with a statistical error > 10 %. The noisy zones above 5000 m, around noon mark the increase in statistical error due to the solar background during the daytime. The white zones mark data gaps.